Pressure Distribution in Various Chamber Shapes of an Aerostatic Thrust Bearing Orifice under High Rotational Speeds

Tayeb Trari
Laboratory of Aeronautics and Propulsion Systems, Faculty of Mechanics, University of Science and Technology of Oran - Mohammed Boudiaf, B.O. Box 1505, El-M'Naouer, 31000, Oran, Algeria | Tissemsilt University- Ahmed Ben Yahia Elwancharissi, Tissemsilt, Algeria
trari.tayeb@univ-tissemsilt.dz

Faiza Ghezali
Structural and Solid Mechanics Laboratory (LMSS), Department of Mechanical Engineering, University Djillali liabes, BP 89,22000, Sidi Bel Abbes, Algeria
ghezali.f18@gmail.com (corresponding author)

Abdelkrim Benlefki
Laboratory of Applied Mechanics, Faculty of Mechanics, University of Science and Technology of Oran - Mohammed Boudiaf, B.O. Box 1505, El-M'Naouer, 31000.Oran, Algeria | Faculty of Sciences and Technology, Tissemsilt University- Ahmed Ben Yahia Elwancharissi, Tissemsilt, Algeria
benlefki.abdelkrim@univ-tissemsilt.dz

Tayeb Yahiaoui
Laboratory of Aeronautics and Propulsion Systems, Faculty of Mechanics, University of Science and Technology of Oran - Mohammed Boudiaf, B.O. Box 1505, El-M'Naouer, 31000, Oran, Algeria
yahiaoui_tayeb@yahoo.fr

Received: 16 March 2025 | Revised: 9 April 2025 | Accepted: 15 April 2025

ABSTRACT

The purpose of this article is to evaluate the impact of air film thickness and chamber shape on the performance characteristics of an aerostatic thrust bearing operating at ultra-high rotational speeds, including pressure distribution, mass flow rate, load capacity, and stiffness. A three-dimensional Reynolds-averaged Navier-Stokes (RANS) analysis using the SST-*k*ω model is employed to study the effect of supply pressure on various operational and geometric parameters. A comparison between the numerical simulation and experimental data was conducted for chamber shape A to verify the model's robustness. Both approaches demonstrated good agreement. Pressure distribution and mass flow were examined across different chamber geometries, revealing the presence of inertia effects and gas vortices, which diminish as the air film thickness increases. Further investigation showed that the load capacity of the aerostatic thrust bearing decreases slightly as the rotational speed increases. Additionally, the numerical results indicate significant variations in the performance of the aerostatic thrust bearing depending on the geometry of the orifice chamber.

Keywords-chamber shapes; aerostatic bearing; film thickness; rotational speed

I. INTRODUCTION

Numerous studies have been conducted to understand the flow behavior within hydrostatic recesses. The classical Reynolds equation, along with its modified forms, has served as the foundation for most recent investigations, particularly those considering turbulence and variations in flow properties. In both numerical and experimental research, key operational parameters, such as shaft speed, inlet jet pressure, and Reynolds number, have been thoroughly examined [1–3]. Authors in [4] investigated the influence of pocket depth and operating conditions on the performance of hydrostatic bearings. They numerically predicted the pressure distribution by solving the two-dimensional Navier-Stokes equations for laminar and incompressible flow. They focused on identifying the nature and location of recirculation zones within the recess and examining their effect on the circumferential flow rate. They observed that the interaction between pressure distribution, flow pattern, and operating conditions becomes significantly more pronounced in deep pockets compared to shallow ones. Authors in [5] introduced fully three-dimensional Navier-Stokes calculations to model the laminar flow of an incompressible fluid within the deep recess of a hydrostatic bearing. In this configuration, the jet flow driven by the supply pressure dominated the behaviour within the recess, while Couette flow prevailed due to shaft rotation. For jet-dominated cases, the pressure inside the pocket remained nearly constant, except at the recess edges where a sharp pressure drop was observed, attributed to the Rayleigh step effect. Additional studies have further contributed to understanding the energy characteristics of hydrostatic bearings. Authors in [6, 7] presented three-dimensional models of laminar and incompressible flow in shallow pockets with varying height-to-width aspect ratios, and simulated the resulting pressure distributions under different operating conditions. Unlike deep pockets, their findings showed that pressure within the shallow recess could no longer be assumed constant. There has been a growing interest in improving the modeling of flow within hydrostatic pockets using three-dimensional Navier-Stokes equations [8–10], aiming to achieve a more accurate understanding of the flow physics in the recess. The key parameters explored in these studies include supply pressure, lubricant film thickness, film size, and recess depth, and their influence on the pressure distribution in hydrostatic thrust bearings. The findings indicate that increasing the film size leads to a reduction in stiffness, while a deeper recess tends to produce more uniform pressure fields. Moreover, results concerning the influence of viscosity suggest that the pressure within the orifice chamber does not decrease smoothly; instead, a Rayleigh step effect occurs. As a result, load capacity increases and the film thickness outside the orifice chamber is altered. Authors in [11] investigated how operating conditions, geometric parameters, and manufacturing errors affect the angular stiffness of aerodynamic bearings. They found that angular stiffness increases with greater eccentricity.

Rotating mechanisms have experienced a significant increase in power-to-mass ratio, leading to smaller sizes and higher rotational speeds. The use of conical bearings has proven to be an effective approach to enhancing mechanical performance. Authors in [12] reported that multilobe conical bearings exhibit improved dynamic stability.

The objective of the present study is to gain a deeper understanding of phenomena occurring within the lubricating film, such as inertia effects and the Rayleigh step at the orifice boundary. Numerical simulation models of various chamber geometries are developed using a three-dimensional CFD approach to analyse the fluid field. To validate the accuracy of the model, the numerical results are initially compared to the experimental data for geometry A. Two key parameters supplying pressure and film thickness are selected to evaluate the performance of the three proposed geometries. The study investigates pressure distribution, load capacity, and air film stiffness across different chamber shapes under a range of rotational speeds.

II. AEROSTATIC BEARING DESCRIPTION

Figure 1 describes the three geometries of aerostatic thrust bearing proposed in this study. As shown in Figure.1, the aerodynamic thrust bearing areas have the following dimensions: the inner diameter (d_{in}) is 23 mm and the outer diameter (d_{out}) is 40 mm. The backward and forward circles of orifice restrictors have a diameter of $d_1 = 28.7$ mm and $d_2 = 29.3$ mm, respectively. Other main dimensions of the configurations are noticed in Table I.

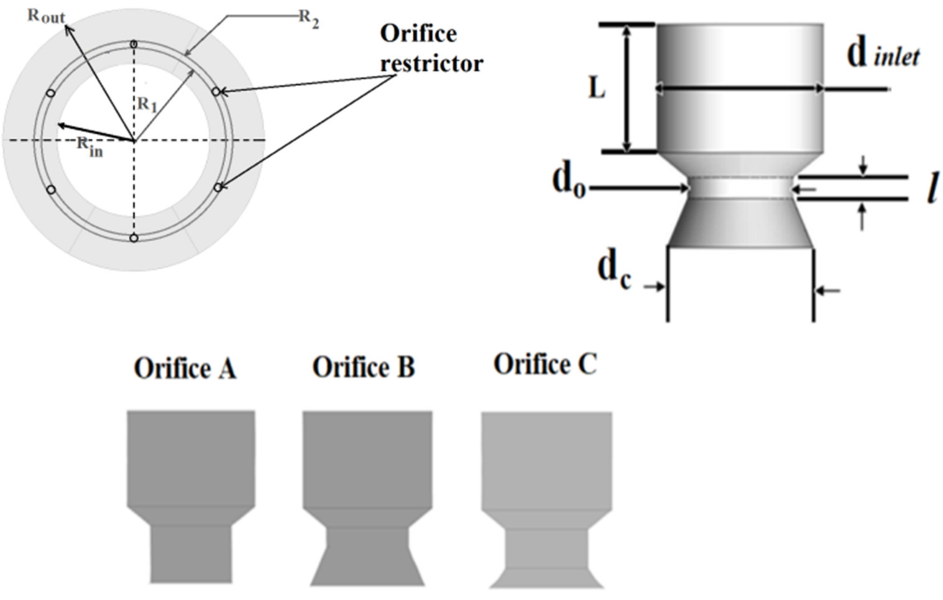

Fig. 1. Illustration of the aerostatic thrust bearing.

TABLE I. GEOMETRICAL CHARACTERISTICS OF AEROSTATIC THRUST BEARING

Geometrical characteristics (mm)		**Orifice type**		
		Orifice A	Orifice B	Orifice C
Orifice length inlet	L (mm)	1.2	1.2	1.2
Orifice length	l (mm)	/	0.1	0.2
Gas inlet diameter	d_{inlet} (mm)	0.7	0.7	0.7
Orifice diameter	d_o (mm)	0.4	0.4	0.4
Chamber diameter	d_c (mm)	0.6	0.6	0.6

For an incompressible and isoviscous lubricant film, both the density and the dynamic viscosity (μ) are constant. Since the plates are parallel, the film thickness (h) is also assumed to be constant. The stiffness of the thrust bearing, defined as the rate of change of load capacity with respect to film thickness, is determined by:

$$\lambda = -\frac{\partial W}{\partial h} = -\frac{\partial W}{\partial P_c}\frac{\partial P_C}{\partial h} \tag{1}$$

The stiffness can be described as:

$$\lambda = -\frac{3W}{h}\left(1 - \frac{\beta}{2-\beta}\right) \tag{2}$$

where β is the pressure rotation equal to P_c/P_s, P_S is the supply pressure, P_C is the orifice chamber pressure, h is the film thickness.

The load capacity is:

$$W = P_c\, S\, K_w \tag{3}$$

In the case where the thrust bearing includes a central circular orifice of radius R, and the pressure at the orifice is equal to ambient pressure, the load capacity can be expressed as: $S = \pi(R_e^2 - R_i^2)$ is the area of thrust bearing, and K_w is the load capacity coefficient.

$$K_w = \frac{1}{2(R_e^2 - R_i^2)}\left[\frac{R_e^2 - R_2^2}{\ln R_e/R_2} - \frac{R_1^2 - R_i^2}{\ln R_1/R_i}\right] \tag{4}$$

III. MESH AND NUMERICAL ANALYSIS

In this study, the three-dimensional steady incompressible RANS equations were solved by ANSYS CFX. The equations were closed using the SST $k-\omega$ turbulence model represented in [13].

Continuity equation can be expressed as:

$$\frac{\partial u_i}{\partial x_j} = 0 \tag{5}$$

Momentum equations can be expressed as:

$$\rho\frac{\partial(u_i u_j)}{\partial x_i} = -\frac{\partial P}{\partial x_i} + \frac{\partial}{\partial x_i}\left[\mu\left(\frac{\partial u_j}{\partial x_i} + \frac{\partial u_i}{\partial x_j} - \frac{2}{3}\delta_{ij}\frac{\partial u_k}{\partial x_k} - \overline{\rho u_i' u_j'}\right]\right. \tag{6}$$

where $\overline{\rho u_i' u_j'}$ is the Reynolds stress.

A steady state approach was utilized to perform numerical simulations on unstructured grids using the commercial code ANSYS CFX19.2. Closure of Reynolds averaged equations (RANS) is achieved through shear stress transport (SST-Kω). This model was chosen because it provides highly accurate predictions of the onset and amount of flow separation under adverse pressure gradients [5]. A close view of the computational unstructured grid at $H = 0.25$ μm , demonstrates that gridding was achieved by the ICEM-CFD mesh generator, which is included in the CFX-19.2 software. In addition to the outlet of the orifice and near the rotational wall of the thrust bearing, the grid is focused on the beginning of the thin film region to resolve the pressure pattern in this region.

Regarding the boundary conditions, as displayed in Figure 2, all orifice surfaces are treated as walls that satisfy adiabatic and no-slip conditions. The rotational speed boundary condition is applied to the rotating wall. At the orifice inlet, a constant static pressure supply is imposed, along with a laminar flow regime. At the outlet, the reference pressure is set to absolute zero (Pa).

Due to the symmetry of the flow at the ends of the model, only one-sixth of the geometry in the radial direction is considered, and a symmetry boundary condition is applied. Convergence was achieved when the residuals of all flow variables (u, v, w, and p) fell below 10^{-5}.

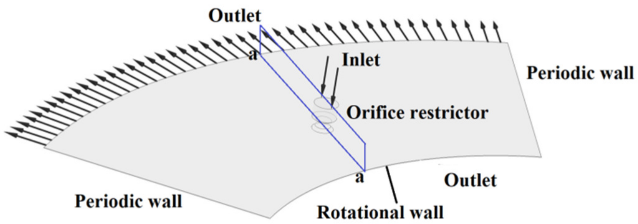

Fig. 2. Perspective views of the computational domain done with the ICEM.CFD.

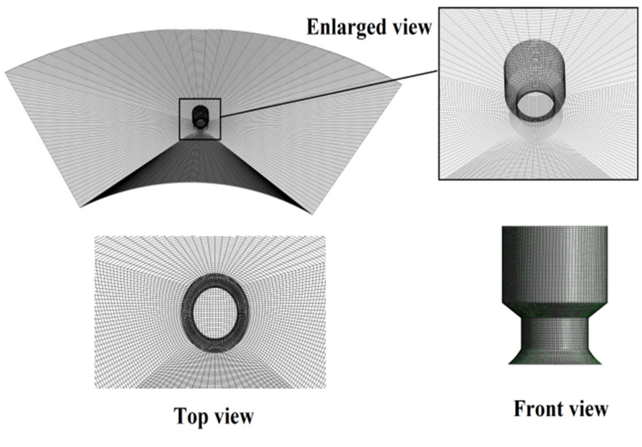

Fig. 3. Illustration of computational meshes.

Figure 3 portrays the computational domain used in this study. Initially, a grid independence test was performed by evaluating three different mesh densities for chamber shape A at a rotational speed of 200.000 rpm and a pressure ratio of $\beta =$

0.998. As illustrated in Figure 4, the results obtained using meshes with 1.8×10^5 and 2.3×10^5 elements were nearly identical. Therefore, the mesh with 1.8×10^5 elements was selected as the optimal grid size.

The total number of elements and nodes used in this configuration were 180,342 and 145,540, respectively. The three chamber shape models, labelled as A, B, and (c), correspond to those presented earlier in Figure 1.

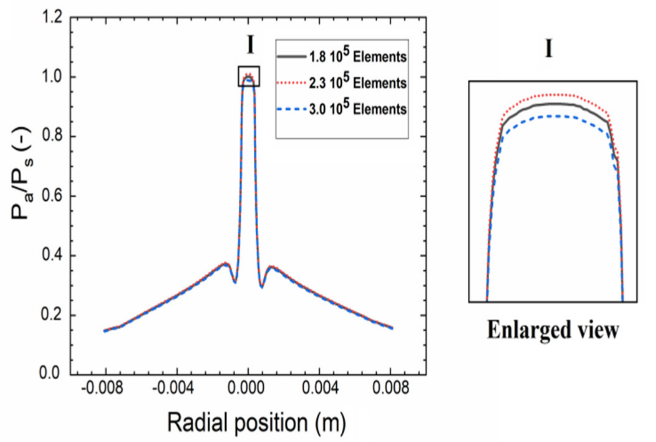

Fig. 4. Mesh independence verification at N = 200.000 rpm and β = 0.998.

IV. NUMERICAL RESULTS

To verify the robustness of the CFD model, the numerical results were compared with the experimental data in [14], using identical geometrical and operational parameters. As presented in Figure 5, the numerical values generally agree well with the experimental data, except in the region near the orifice. This discrepancy is attributed to the difficulty of experimentally measuring the pressure directly beneath the orifice.

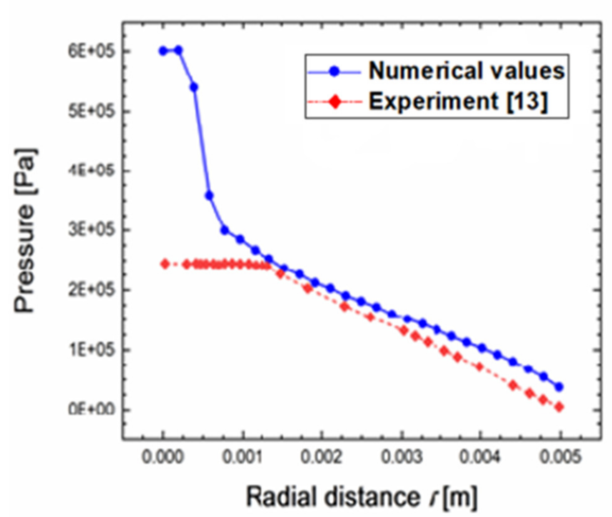

Fig. 5. Comparison of radial pressure distribution between numerical values and experimental data of orifice restrictor C.

A. *Effect of Film Thickness and Chamber Shapes at Pressure Distributions*

The pressure distributions in the radial direction along the line, as depicted in Figure 6, for various chamber shapes, with respect to two values of air film thickness H = 25 μm and H = 17μm at a speed of 200,000 rpm are, respectively, illustrated in Figure 7. It is observed that as the thickness of the air film decreases, the pressure of the air film increases accordingly. The maximum pressure of the air film has been discovered to be located at the center of the orifice outlet, and it gradually decreases to ambient pressure along the radial direction. Pressure depression, pressure drop, and recovery effects occur in the gas film, which can decrease the load capacity of the air film.

By comparing the pressure levels in the radial direction of line a–a, it is noted that the operating speeds demonstrated in Figure 7 are displayed for chamber shapes with air film thicknesses of 25 μm and 17 μm. The value of pressure distributions differs significantly for different types of chamber shapes. The pressure ratio increased from 0.1 to 0.35 as the film thickness reduced from 25 μm and 17 μm around the orifice exit diameter, and atmospheric pressure reached the outlet of the aerostatic bearing. Orifice B has close values around it, and the pressure ratio dropped from 0.21 to 0.1 due to the increase in film thickness from 25μm and 17 μm at the bearing outlet. Regarding orifice C, the behavior of pressure fields differs from that of other configurations. With the film thickness decreasing, the pressure ratio between the orifice and bearing exit ranged from 0.25 to 0.4 and from 0.2 to 0.12, respectively. This result is a consequence of the inclination effect caused by the shape of the exit of the orifice chambers.

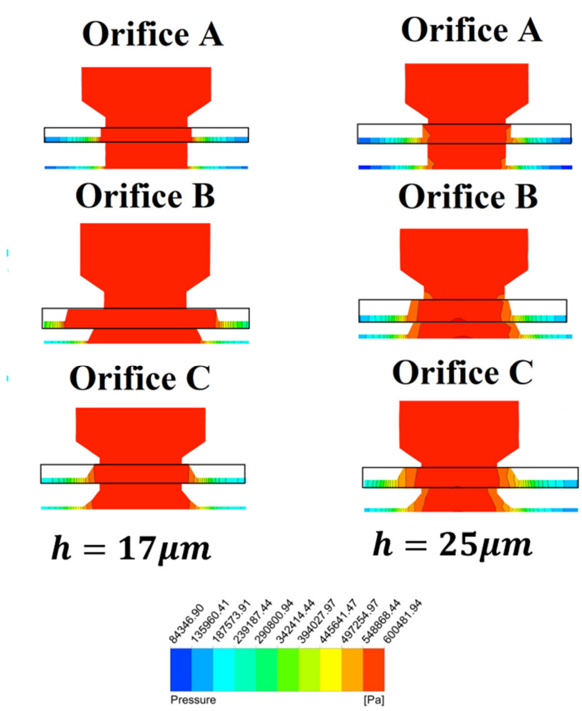

Pressure distributions in the three chamber shapes at N=200,000 rpm, H = 17 μm and H = 25 μm.

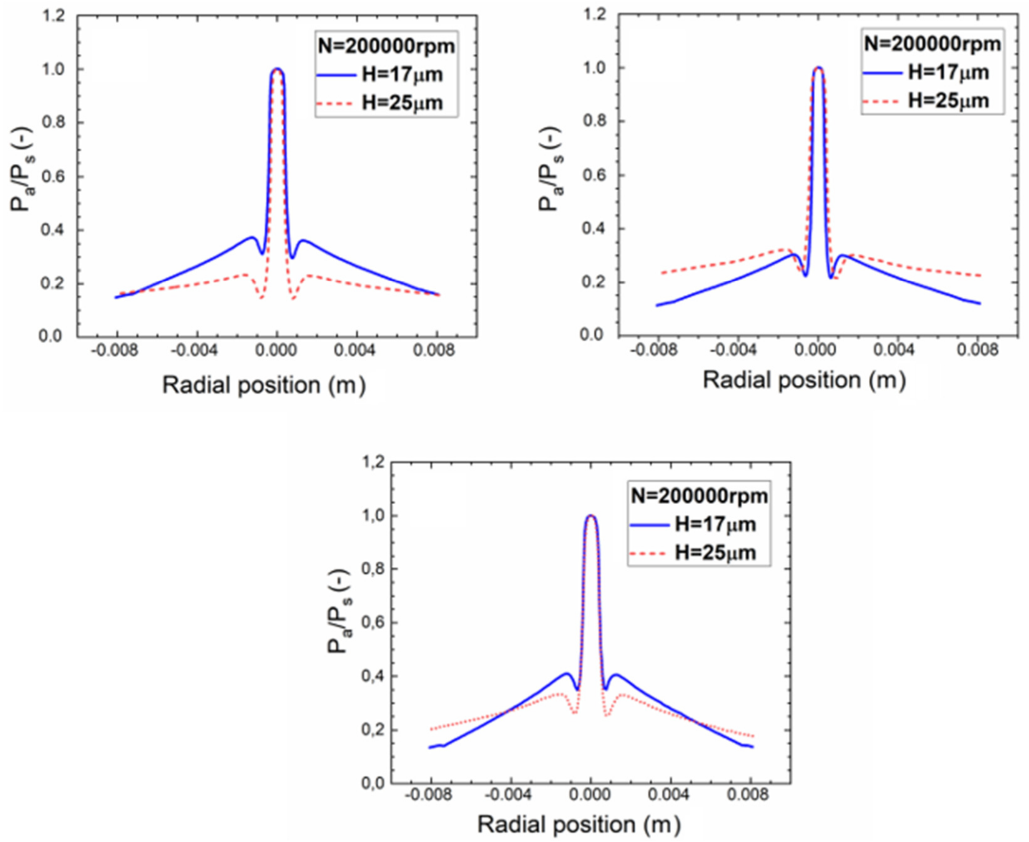

Fig. 6. Comparison of pressure ratio distributions for various chamber shapes and film thickness at N = 200000 rpm.

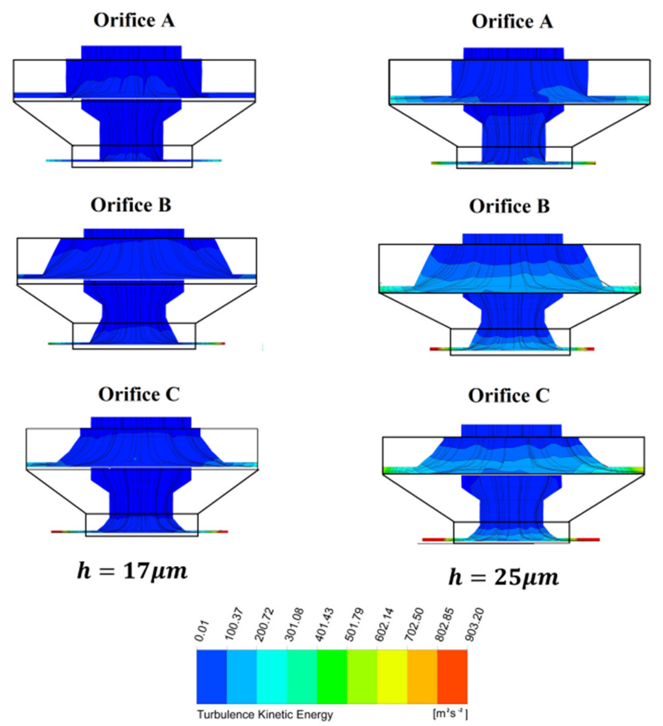

Fig. 7. Turbulence kinetic energy at N = 200,000 rpm for H = 25 μm and 17 μm.

The proposed configurations influence the variation of the local turbulent kinetic energy, as depicted in Figure 8. Chamber type A, B, and C sequences have a local turbulent kinetic energy increase, with an air film thickness range between 17 μm and 25 μm. This is essentially due to the exit orifice chamber. The first configuration A has a strong deviation in film thickness. For the second configuration "B", the cone diminishes the deviation by approximately 50% in comparison to the shape "A". The third one "C" has a smooth deviation in comparison to other outlet chamber shapes.

Figure 9 presents a comparison of the pressure ratio for different film thicknesses and chamber shapes at a rotational speed of N=200,000 rpm. For regions outside the chambers, the pressure in chamber type A reaches atmospheric levels at both H = 17 μm, h = 25 μm. It is also observed that chamber shape A exhibits lower pressure compared to the other configurations at H = 25 μm, and an inertia effect is noticeable around the injection zone. Chamber type C shows the highest pressure ratio overall, while type B displays nearly identical pressure values across different film thicknesses.

B. *Effect of Rotational Speed in Pressure Distribution*

The chamber type A is used to simulate the pressure ratio of the air film for various chamber shapes at different operating rotational speeds. Figure 10 demonstrates the pressure distributions (along the line a–a) of type A for the air film thickness of 25 μm when rotating at different speeds. It is apparent that aerostatic bearing pad pressures remain consistent regardless of the rotational speed, and the peak pressure around the injection zone increases with the rotational speeds. Furthermore, the pressure distributions outside the chamber almost remain unchanged at different operating speeds.

C. Effect of Film Thickness and Rotational Speed on Load Capacity

Figure 11 (a) illustrates the influence of air film thickness on the load capacity for various chamber shapes at an operating speed of 200,000 rpm. The results show that load capacity decreases as air film thickness increases for all chamber configurations. This behavior is attributed to the pressure drop within the air film as its thickness increases, as also shown in Figure 6. Among the tested geometries, chamber type A consistently exhibits lower load capacity compared to the others. At a film thickness of 13 μm, the load capacities of chamber types A and B are nearly identical. Similarly, at 25 μm, the load capacities of types B and C are comparable. However, across the film thickness range of 13–25 μm, chamber type B shows slightly lower load capacity than type C.

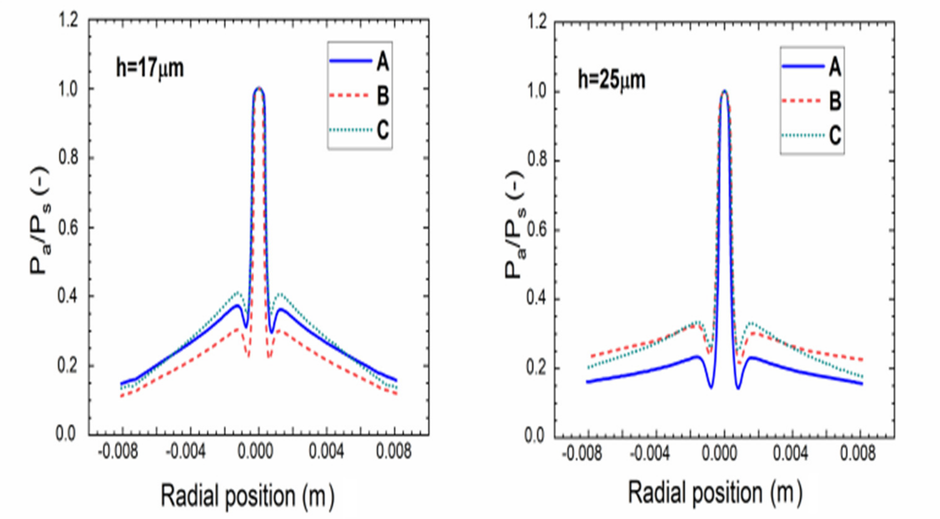

(a) (b)

Fig. 8. Comparison of pressure distributions for various chamber shapes at N = 200,000 rpm, film thickness: (a) H = 25 μm and (b) h = 17 μm.

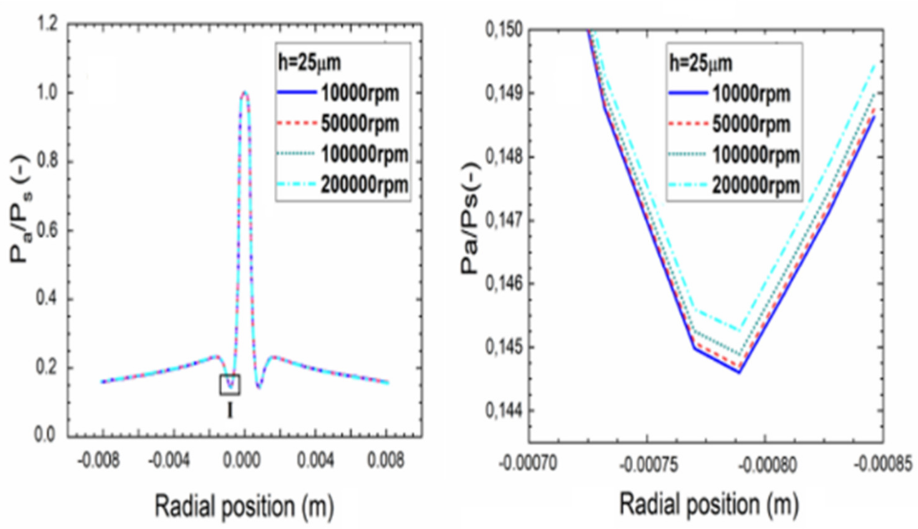

(a) (b)

Fig. 9. Pressure ratio at various rotational speeds for chamber type A (h = 25 μm), (a) general view and (b) enlarged view.

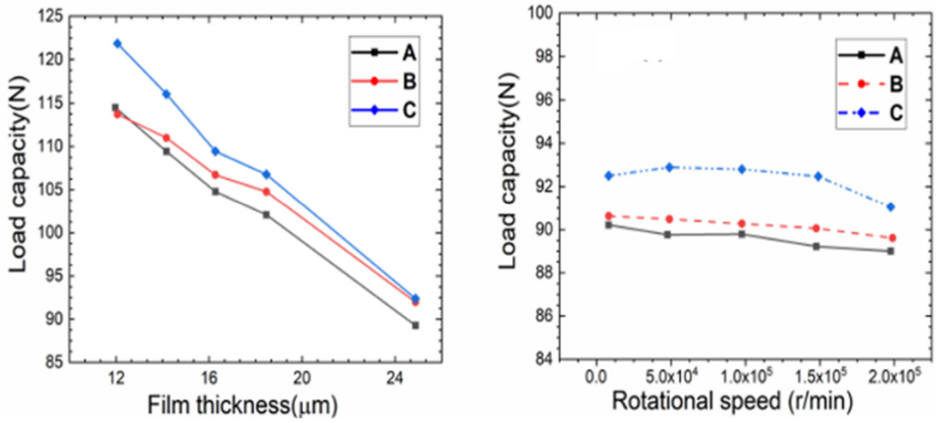

(a) (b)

Fig. 10. Load capacity for various chamber shapes, (a) N = 200,000 rpm, (b) H =25 μm.

Figure 11(b) presents the variation of load capacity with rotational speed for different chamber shapes at a constant film thickness of H = 25 μm. The results indicate a slight decrease in load capacity for each chamber as rotational speed increases. This reduction is mainly due to a drop in the average pressure within the air film, with the Bernoulli effect becoming more dominant at higher rotational speeds.

V. CONCLUSION

In this study, a three-dimensional CFD model was developed using ANSYS CFX to investigate the influence of rotational speed and film thickness on the pressure field of an aerostatic thrust bearing supplied by an orifice restrictor. The analysis focused on how three different orifice chamber geometries affect the key performance characteristics of the bearing under ultra-high-speed operating conditions.

The results demonstrate that chamber geometry plays a crucial role in ensuring effective shaft lubrication. Rotational speed was found to gradually affect the pressure distribution on the aerostatic pad, creating a transitional zone between low and high pressure at the boundary of the injection area. A distinct pressure peak consistently appears at the center of the orifice across all configurations and operating conditions. Furthermore, as the rotational speed increases, the load capacity of the air film tends to decrease across all chamber types. Although the overall performance of the three geometries is comparable over the tested film thickness range, a gradual reduction in load capacity is observed from chamber A to chamber C. Each configuration exhibits different behaviour in terms of load capacity and stiffness as rotational speed varies, with chamber C emerging as the most suitable for high-load applications due to its superior pressure recovery at reduced film thickness.

To maintain effective lubrication, the air film should not be excessively thick. It was observed that increasing film thickness results in a pressure drop and amplifies the inertia effect near the injection zone, ultimately reducing the load capacity. This research contributes to a deeper understanding of the flow behavior in orifice-type aerostatic thrust bearings and opens new perspectives for standardizing pressure distribution in the orifice feedline. Such optimization can enhance the operational stability and improve the performance of aerostatic bearings in terms of both load capacity and lubricating film stiffness.

REFERENCES

[1] J. K. Scharrer and R. I. and Hibbs Jr., "Flow Coefficients for the Orifice of a Hydrostatic Bearing," *Tribology Transactions*, vol. 33, no. 4, pp. 543–550, Jan. 1990, https://doi.org/10.1080/10402009008981987.

[2] I. Pierre and M. Fillon, "Influence of geometric parameters and operating conditions on the thermohydrodynamic behaviour of plain journal bearings," *Proceedings of the Institution of Mechanical Engineers, Part J: Journal of Engineering Tribology*, vol. 214, no. 5, pp. 445–457, May 2000, https://doi.org/10.1243/1350650001543322.

[3] V.-H. Pham, M.-T. Nguyen, and T.-A. Bui, "Oil pressure and viscosity influence on stiffness of the hydrostatic spindle bearing of a medium-sized circular grinding machine," *International Journal of Modern Physics B*, vol. 34, no. 22–24, Sep. 2020, Art. no. 2040156, https://doi.org/10.1142/S0217979220401566.

[4] M. J. Braun and M. Dzodzo, "Effects of the Feedline and the Hydrostatic Pocket Depth on the Flow Pattern and Pressure Distribution," *Journal of Tribology*, vol. 117, no. 2, pp. 224–232, Apr. 1995, https://doi.org/10.1115/1.2831233.

[5] M. J. Braun and M. B. Dzodzo, "Three-Dimensional Flow and Pressure Patterns in a Hydrostatic Journal Bearing Pocket," *Journal of Tribology*, vol. 119, no. 4, pp. 711–719, Oct. 1997, https://doi.org/10.1115/1.2833875.

[6] S. K. Kakoty and B. C. and Majumdar, "Effect of Fluid Film Inertia on Stability of Flexibly Supported Oil Journal Bearings: A Non-Linear Transient Analysis," *Tribology Transactions*, vol. 45, no. 2, pp. 253–257, Jan. 2002, https://doi.org/10.1080/10402000208982548.

[7] Y. Zhou, X. Chen, Y. Cai, H. Chen, and B. Han, "Measurement of gas pressure distribution in aerostatic thrust bearings using pressure-sensitive film," *Tribology International*, vol. 120, pp. 9–15, Apr. 2018, https://doi.org/10.1016/j.triboint.2017.12.002.

[8] J. Zhang, D. Han, M. Song, Z. Xie, Z. Rao, and D. Zou, "Theoretical and experimental investigation on the effect of supply pressure on the nonlinear behaviors of the aerostatic bearing-rotor system," Mechanical Systems and Signal Processing, vol. 158, Sep. 2021, Art. no 107775, https://doi.org/10.1016/j.ymssp.2021.107775.

[9] P. B. Kushare and S. C. Sharma, "Nonlinear transient stability study of two lobe symmetric hole entry worn hybrid journal bearing operating with non-Newtonian lubricant," *Tribology International*, vol. 69, pp. 84–101, Jan. 2014, https://doi.org/10.1016/j.triboint.2013.08.014.

[10] A. Walicka, E. Walicki, P. Jurczak, and J. Wojnarowski, "Mechanical Parameters for a Multilobe Conical Bearing Lubricated with a Couple-

Stress Fluid," *Machine Dynamics Research*, vol. 39, no. 4, pp. 43–54, 2015.

[11] H. Cui *et al.*, "Numerical analysis and experimental research on the angular stiffness of aerostatic bearings," *Tribology International*, vol. 120, pp. 166–178, Apr. 2018, https://doi.org/10.1016/j.triboint.2017.12.040.

[12] A. K. Gangrade, V. M. Phalle, S. S. Mantha, and A. N. Siddiquee, "Influence of eccentricity ratio on stability performance of hydrodynamic conical journal bearing," *Journal of Physics: Conference Series*, vol. 1240, no. 1, Apr. 2019, Art. no. 012115, https://doi.org/10.1088/1742-6596/1240/1/012115.

[13] G. Belforte, T. Raparelli, V. Viktorov, and A. Trivella, "Discharge coefficients of orifice-type restrictor for aerostatic bearings," *Tribology International*, vol. 40, no. 3, pp. 512–521, Mar. 2007, https://doi.org/10.1016/j.triboint.2006.05.003.

[14] F. Menter, M. Kuntz, and R. Langtry, " Ten Years of Industrial Experience with the SST Turbulence Model," in *4th Internal Symposium, Turbulence, heat and mass transfer*, Antalya, Turkey, 2003, pp. 625-632.